

Fractional corner charges induced by fragile topology in threefold symmetric two-dimensional materials

Olga Arroyo-Gascón,^{1,2} Sergio Bravo,³ Leonor Chico,² and Mónica Pacheco³

¹*Instituto de Ciencia de Materiales de Madrid, Consejo Superior de Investigaciones Científicas, C/ Sor Juana Inés de la Cruz 3, 28049 Madrid, Spain*

²*GISC, Departamento de Física de Materiales, Universidad Complutense, E-28040 Madrid, Spain*

³*Departamento de Física, Universidad Técnica Federico Santa María, Casilla 110-V, Valparaíso, Chile*

(Dated: December 15, 2023)

We perform a systematic study of the signatures of fragile topology in a number of nonmagnetic two-dimensional materials belonging to space group 164, most of them transition metal dichalcogenides. Using group theory analysis in the framework of topological quantum chemistry, we find fragile bands near the Fermi level for all the materials studied. Since stable topological bands are also present in these systems, the interplay of both phases is discussed, showing that corner charges appear in nearly three quarters of the materials and that they are caused by fragile topology. Using first-principles calculations, we predict corner states with fractional corner charges protected by C_3 symmetry. Our work aims to broaden the scope of materials with experimentally accessible fragile bands.

I. INTRODUCTION

Since the proposal and later discovery of the first topological insulators, topology has enriched the electronic properties of a great number of materials. Different types of Dirac and Weyl fermions have been discovered in analogy to high-energy physics. The development of symmetry indicators and topological quantum chemistry [1–5] has further extended and standardized the variety of topological phases of matter. Higher-order topological insulators (HOTI) and fragile topology are the latest additions; the former was first established in topological insulators protected by a mirror Chern number [6], while the latter has appeared in twisted bilayer graphene [7–9]. Both phases share the absence of topological gapless modes on their surfaces or edges, in contrast to standard topological insulators. Whereas HOTIs of d -dimension are known to host topological states in $d - 2$ dimensions, the same does not always apply to fragile topology. Interestingly, while nearly 90% of all materials have at least one topological band [1], only about 8% show fragile states. Thus, the search for new materials that could provide more information on signals of fragile topology is highly desirable.

Fragile topology is based on the fact that fragile bands can be trivialized by adding more orbitals. In the framework of topological quantum chemistry (TQC), the band structure of any material is described by elementary band representations (EBRs), induced from the symmetries of the space group of the material [2, 3, 10]. A band is said to be topologically trivial if it admits a rewrite in terms of EBRs using only integer positive coefficients [2, 3]. Then, the symmetry operations of each subgroup of the material space group at high-symmetry points, called irreducible representations (irreps), match those of the EBRs involved in the linear combination. Unlike trivial bands, fragile bands can be expressed as a combination of EBRs with integer coefficients, but at least one of them must

be negative [2]. This way, when more bands are added to a fragile one, the negative EBRs can cancel out, giving rise to an all-positive linear combination of EBRs and thus trivializing the band set. Hence, even if the fragile state is near the Fermi energy, the lower energy bands can trivialize it. This trivialization can explain the scarcity of topological materials with fragile topology features.

Fragile topology cannot be captured by the well-known \mathbb{Z}_2 invariant, and fragile bands also have $\mathbb{Z}_4 = 0$. There are no measurable surface states related to this kind of topology. Therefore, topological quantum chemistry stands as a suitable tool for diagnosing these states. A non-trivial topology can also be described by Wilson loop calculations, studying the winding of the Wannier charge centers [7, 11, 12]. In order to have a complete picture of fragile topological materials, a complete study of fragile bands for all space groups in the framework of TQC has been performed in Ref. [13]. However, to our knowledge, there is no two-dimensional database of fragile topology.

Fragile topology has also been reported in photonic crystals and phonon spectra [14–16]. Its main signature is the presence of zero-dimensional corner states with corner charges in a two-dimensional system, theoretically predicted in Refs. [9, 17, 18]. These corner charges have been theoretically reported in recent works studying different mono- and few-layered materials with diverse rotational symmetries [19–24]. Moreover, higher-order Fermi arcs have also been linked to fragile and higher-order topology in some transition-metal dichalcogenides [25]. From an experimental point of view, fragile topology has been described in metamaterials [26], and Fermi arcs have been reported in some transition-metal dichalcogenides [27–29]. Because corner charges are a shared feature between fragile and higher-order topology, corner state measurements in real materials are often linked to the latter [30].

It is therefore interesting to study the relation between higher-order and fragile topology. In this direction, we construct a list of two-dimensional monolayers described

by space group 164 ($P\bar{3}m1$). Since transition-metal dichalcogenides (TMDs) have received a great deal of attention as candidates for layered materials with higher order [20, 31–34] and fragile topology [20, 25], we have focused on various TMDs, as well as on a number of non-TMDs with the same space group. We explore a total of 24 materials to find a set of experimentally suitable candidates. We demonstrate that fragile topological bands are present in all 24 materials in the valence region near the Fermi level, and that these bands are responsible for the non-zero corner charges present in most of the materials and in C_3 -symmetric flakes.

This paper is organized as follows: In Section II, the general properties of space group 164 and the materials therein are discussed. In Section III, we compute a set of topological invariants based on the symmetry eigenvalues of the system, particularized to the case studies ZrSe_2 , ZrS_2 and, SnS_2 . In Section IV, we theoretically predict the corner charges linked to these materials and present the concept of partial corner charge. Our results are consistent with first-principles corner states calculations for triangular and hexagonal flakes in Section V.

II. COMPUTATIONAL METHODS AND GENERAL BACKGROUND OF SPACE GROUP 164 MATERIALS

Electronic structure calculations for all materials were performed using the Quantum ESPRESSO first-principles code [35, 36] employing the generalized gradient approximation (GGA) and Perdew–Burke–Ernzerhof (PBE) exchange–correlation functionals. Spin-orbit coupling was considered throughout the self-consistent calculations in all cases. A kinetic energy wavefunction cutoff of 100 Ry and a $8 \times 8 \times 1$ Monkhorst-Pack reciprocal space grid were used. All structures were relaxed until the forces were less than $0.001 \text{ eV}/\text{\AA}$. The initial crystal structures were obtained from the Computational 2D Materials Database (C2DB) [37, 38] and checked against the Topological Materials Database [1, 10, 39] for further relaxation.

Subsequently, a group theory analysis was performed using the IrRep code [40]. For the flake calculations, the SIESTA code [41, 42] was used, including spin-orbit coupling and considering the same GGA-PBE approximation.

Space group (SG) 164 ($P\bar{3}m1$) has inversion symmetry and includes rotational symmetries C_{3z} and C_{2x} , with a total of 12 symmetry operations. As shown in Figures 1 (a) and (b), we focus on AB_2 compounds that display a layered structure. The A atom, which is usually but not necessarily a transition metal, belongs to the high-symmetry real space Wyckoff position (WP) 1a, whereas the B atom is described by the 2d WP. The spatial location of these positions within the unit cell is highlighted in blue and orange, respectively, in Figure 1 (a). For the WPs, as well as for the symmetry operations and the

space group, we are following the notation of the Bilbao Crystallographic Server [43–45].

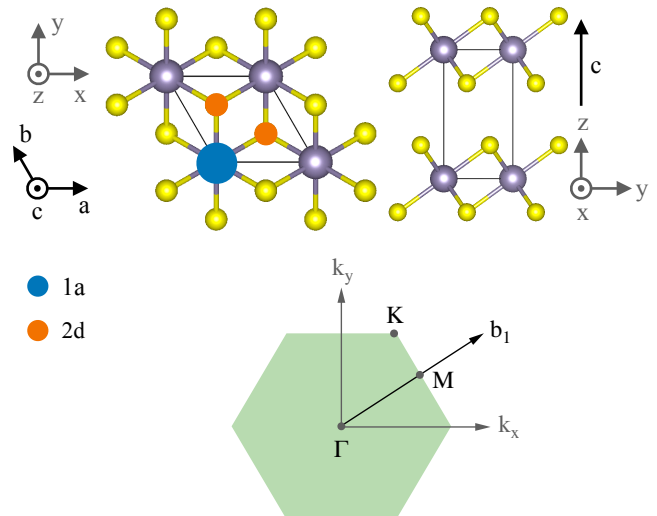


FIG. 1. Crystal structure of a unit cell belonging to SG 164: (a) top view, and (b) side view displaying two layers. The structure lattice vectors, as well as the cartesian axes, are indicated in black and grey, respectively. Blue and orange highlighted atoms indicate the 1a and 2d WPs, respectively. (c) Brillouin zone of the monolayer.

We screen the C2DB by restricting the search to dynamically stable monolayers with SG 164 and AB_2 formula that possess a PBE band gap with a magnitude greater than 0.1 eV and a nonmagnetic ground state. Additionally, we also mention examples of semimetallic systems that allow for a formal definition of a set of valence bands separated from the upper conduction bands by a non-absolute gap. From an experimental point of view, a sizeable band gap is beneficial, since the potential corner states will not be hindered by edge states. Although topological features have been described and measured in some of these compounds, fragile topology has not been studied yet in any of these materials. A complete list of materials identified in this work is presented in Table III.

In the following sections we will focus on three illustrative materials of this collection that have already been synthesized in monolayer form [46–48], namely, ZrSe_2 , ZrS_2 , and SnS_2 . The semimetals ZrTe_2 and NiTe_2 are also briefly commented, and the particularities of their response in comparison with the insulating cases are discussed. In addition to the aforementioned compounds, other materials encompassed in this work such as PtSe_2 , SnI_2 or PbI_2 are also experimentally available as monolayers.

III. BAND TOPOLOGY CHARACTERIZATION

A. Topological quantum chemistry analysis

In the context of fragile topology, since other benchmarks of topology, such as surface states, are absent, TQC emerges as one of the most useful methods. We perform a TQC analysis of the individual bands as well as of the general valence band manifold. Note that the fragile topology database described in [13] may not apply here, since in the monolayer case the combination of EBRs is now restricted to the two-dimensional high-symmetry points of the Brillouin zone (BZ).

The basic ingredient to start the topological description is to consider that time-reversal symmetry and spatial inversion are both preserved for all cases. This immediately implies that all energy bands will be twofold degenerate along the entire BZ. In addition, as spin-orbit is not negligible, the double space group irreducible representations should be employed to characterize the bands at high symmetry points. The general feature of this double version for SG 164 is that the highest degeneracy that a set of bands can have is two. Therefore, all doubly degenerate bands will always be isolated from each other. This allows for the topological classification not only of the valence band manifold as a whole, but also for the characterization of each twofold set of bands. This basic set of bands can be described by the labels of the irreps at high symmetry points Γ , M and K , which comprises what is known as a band representation [10].

Following the notation in the Bilbao Crystallographic Server, we list in Table I all possible band representations that are allowed by the compatibility relations of the group. If a set of bands corresponds to a combination of EBRs with integer coefficients and at least one of them is negative, the set is fragile [2]; if at least one is fractional, the set has stable topology. Otherwise, if all coefficients are positive integers, the set is said to be in an atomic limit and trivial [3]. To identify these phases, we follow the Smith decomposition procedure [2] as detailed in the Appendix. We define a topological invariant indicated by symmetry eigenvalues \mathbb{Z}_2 as

$$\mathbb{Z}_2 = c_6 \bmod 2 \quad (1)$$

Where c_6 is the 6-th element of the c -vector, obtained from the multiplicities of the irreps of each band set and whose computation is reported in the Appendix. An example of a $\mathbb{Z}_2 = 1$ stable topological band S is detailed below.

$$S = -\frac{1}{2}{}^1\bar{E}_g{}^2\bar{E}_g@1a + \frac{1}{2}{}^1\bar{E}_g{}^2\bar{E}_g@3e \quad (2)$$

Where \bar{E}_i labels the different EBRs, and 1a and 3e are two different WPs of SG 164, to whom each EBR is linked to (these symmetry positions are said to induce the EBRs). To properly describe the irreps that label the high-symmetry points of band S, we have to resort

to fractional coefficients, which indicates a stable topological phase. We have checked that fragile and $\mathbb{Z}_2 = 1$ bands are present in the valence bands near the Fermi level for all reported materials. A potential interplay between strong, $\mathbb{Z}_2 = 1$ -indicated topological phases and fragile phases and its effect on corner states would be of great interest.

The above-described TQC study of the valence bands yields sixteen basic band representations that can be classified as fragile, stable topological with $\mathbb{Z}_2 = 1$, and trivial, and are gathered in Table I.

	Γ	M	K	$Q_{c,no\ inv}$	$Q_{c,inv}$
EBR	$\bar{\Gamma}_4\bar{\Gamma}_5$	$\bar{M}_3\bar{M}_4$	$\bar{K}_4\bar{K}_5$	0	0
F1	$\bar{\Gamma}_4\bar{\Gamma}_5$	$\bar{M}_3\bar{M}_4$	\bar{K}_6	4/3	2/3
S	$\bar{\Gamma}_4\bar{\Gamma}_5$	$\bar{M}_5\bar{M}_6$	$\bar{K}_4\bar{K}_5$	0	3/2
S	$\bar{\Gamma}_4\bar{\Gamma}_5$	$\bar{M}_5\bar{M}_6$	\bar{K}_6	4/3	1/6
S	$\bar{\Gamma}_6\bar{\Gamma}_7$	$\bar{M}_3\bar{M}_4$	$\bar{K}_4\bar{K}_5$	0	1/2
S	$\bar{\Gamma}_6\bar{\Gamma}_7$	$\bar{M}_3\bar{M}_4$	\bar{K}_6	4/3	7/6
EBR	$\bar{\Gamma}_6\bar{\Gamma}_7$	$\bar{M}_5\bar{M}_6$	$\bar{K}_4\bar{K}_5$	0	0
F2	$\bar{\Gamma}_6\bar{\Gamma}_7$	$\bar{M}_5\bar{M}_6$	\bar{K}_6	4/3	2/3
F3	$\bar{\Gamma}_8$	$\bar{M}_3\bar{M}_4$	$\bar{K}_4\bar{K}_5$	2/3	4/3
EBR	$\bar{\Gamma}_8$	$\bar{M}_3\bar{M}_4$	\bar{K}_6	0	0
S	$\bar{\Gamma}_8$	$\bar{M}_5\bar{M}_6$	$\bar{K}_4\bar{K}_5$	2/3	5/6
S	$\bar{\Gamma}_8$	$\bar{M}_5\bar{M}_6$	\bar{K}_6	0	3/2
S	$\bar{\Gamma}_9$	$\bar{M}_3\bar{M}_4$	$\bar{K}_4\bar{K}_5$	2/3	11/6
S	$\bar{\Gamma}_9$	$\bar{M}_3\bar{M}_4$	\bar{K}_6	0	1/2
F4	$\bar{\Gamma}_9$	$\bar{M}_5\bar{M}_6$	$\bar{K}_4\bar{K}_5$	2/3	4/3
EBR	$\bar{\Gamma}_9$	$\bar{M}_5\bar{M}_6$	\bar{K}_6	0	0

TABLE I. Basic band representations in SG 164 monolayer, including trivial (labelled EBR), stable topological with $\mathbb{Z}_2 = 1$ (labelled S), and fragile (labelled F and numbered). Corner charges with and without inversion symmetry for all nontrivial bands are gathered in the last two columns and described in Section IV.

For example, fragile band F2 can be decomposed into EBRs as shown in Eq. 3 below. Note that these representations are not unique as the general formulation for the symmetry data vector has several free parameters. These parameters are usually set to zero [2]; however, we have checked that other parameter choices do not change the resulting topological nature of each symmetry data vector.

$$F2 = {}^1\bar{E}^2\bar{E}@2d \ominus {}^1\bar{E}_g{}^2\bar{E}_g@1a \quad (3)$$

The negative coefficients confirm the fragile nature of the band, and are also present in the decomposition of the rest of the fragile bands in Table I. In all cases, these fragile bands can be described in terms of EBRs coming from 1a and 2d WPs, which are the occupied sites in the unit cell. From the above expression, the band representation that is induced by orbitals at the 2d WP can be written as $F2 \oplus {}^1\bar{E}_g{}^2\bar{E}_g@1a$. In this form, it can be observed that the EBR contribution is identical to the con-

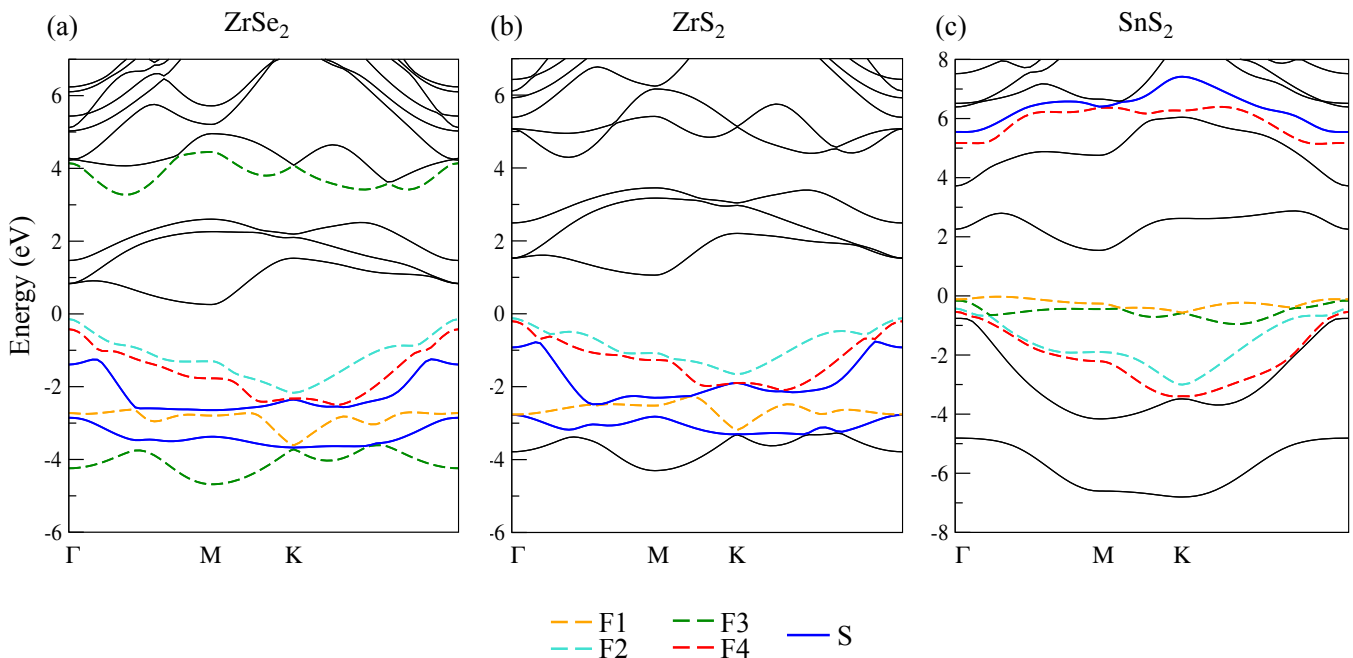


FIG. 2. Band structure of monolayer (a) ZrSe₂, (b) ZrS₂ and (c) SnS₂. Fragile bands are represented in colored dashed lines, and $\mathbb{Z}_2 = 1$ bands are highlighted in dark blue.

tribution coming from orbitals at the 1a WP. Therefore, when considering the interaction process in the material, that is, hybridization of orbitals between 1a and 2a WP, it will be expected that two bands with ${}^1\bar{E}_g {}^2\bar{E}_g @ 1a$ character will arise, since they share the same symmetry. The remaining state induced by this process must be a fragile band. This gives us a baseline argument that hints at the significant presence of fragile bands due to orbital interaction processes.

In light of our preceding general results, we now classify the electronic bands in the representative case studies ZrS₂, ZrSe₂ and SnS₂.

Figure 2 (a) shows the band structure of the monolayer ZrSe₂ near the Fermi level, where a variety of topological bands, both stable and fragile, appear. All types of identified fragile bands F1, F2, F3, and F4, shown in dashed lines and different colors, are present in the valence set near the neutrality point. Stable $\mathbb{Z}_2 = 1$ bands, highlighted in blue, also appear in the valence region and have been generically labeled S for simplicity. If we extend the TQC analysis to the entire valence band set, we find that ZrSe₂ is topologically trivial, as its irreps can be expressed as a sum of different EBRs. This is consistent with the intuitive notion of fragile bands: they are trivialized when combined with other bands. In contrast to fragile bands, the $\mathbb{Z}_2 = 1$ bands remain topological upon addition; the only exception is the addition of an even number of $\mathbb{Z}_2 = 1$ bands, since the \mathbb{Z}_2 index is defined modulo 2. We emphasize that there are more topologically stable and fragile bands at lower energies, which we do not show in the figure but have been taken into con-

sideration in order to compute the topological properties of the valence band set.

ZrSe₂ and ZrS₂ are semiconductors and share almost the same topological band distribution for the uppermost valence bands, as seen in Figure 2 (a) and (b). In both cases, the first, second, and fourth valence bands have fragile topology, and the third and fifth valence bands are stable topological with $\mathbb{Z}_2 = 1$. In fact, the band structure has an overall similar appearance for both materials, as expected since they belong to a similar chemical environment. However, in ZrS₂ there are no topological bands in the conduction set near the Fermi level. As in ZrSe₂, all valence bands add up to a trivial topological invariant.

Figure 2 (c) displays an analogous band structure for the semiconductor SnS₂. As in ZrSe₂, all fragile bands F1, F2, F3, and F4 found in Table I are present in the figure. Interestingly, these valence bands do not include any $\mathbb{Z}_2 = 1$ bands; however, we have found bands with that type of topology at lower energies. As in the previous cases, the whole valence manifold is topologically trivial.

For the rest of the monolayers studied, the results are similar. Additional figures highlighting fragile and stable bands for ZrTe₂ and NiTe₂ are found in the Supplementary Information. They both have a higher density of stable bands but show fragile states near the Fermi level. Since ZrTe₂ and NiTe₂ are semimetals, we have set the uppermost valence band to match previous works [1, 10, 39]. ZrTe₂ is the only one that has a set of topological valence bands $\mathbb{Z}_2 = 1$, but note that this result

depends on the aforementioned choice of occupied bands for the TQC calculation. All the materials mentioned above (ZrSe₂, ZrS₂, SnS₂, ZrTe₂ and NiTe₂) are experimentally feasible in monolayer form. In summary, TQC analysis of these materials yields a broad range of materials with fragile and stable topology.

B. Symmetry-indicator invariants beyond topological quantum chemistry

To study the potential fragile and/or higher-order benchmarks of these systems, two-dimensional flakes are usually proposed as a platform for hosting zero-dimensional states with corner charges. For systems with corner charges, a set of invariants of the symmetry indicator related to rotational symmetries C_n can be defined [18, 19]. Note that these invariants can be applied to both fragile and HOTIs. In the same way, \mathbb{Z} or the Chern number invariants can be computed in terms of inversion or mirror symmetry eigenvalues, these symmetry invariants are defined in terms of the eigenvalues of different rotational symmetries, depending on the system geometry. As commented in Section II, SG 164 has C_2 , C_3 , inversion, and mirror symmetries. Following [19], a spin-orbit coupled system in the presence of C_2 , C_3 and inversion symmetries (that is, with high-symmetry points Γ , M and K) is characterized by the following invariant ν_{inv} :

$$\nu_{inv} = (M_{-1}^I, K_{-1}^3) \quad (4)$$

Where M_{-1}^I is the difference between the number of states at M and Γ points with inversion eigenvalue -1 . Analogously, K_{-1}^3 is the difference between the number of states at K and Γ points with C_3 eigenvalue -1 . If only the C_3 symmetry is considered, the corresponding invariant is

$$\nu_{no\ inv} = (K_{e^{i\pi/3}}^3, K_{-1}^3), \quad (5)$$

where $K_{e^{i\pi/3}}^3$ is the difference of number of states at K and Γ with C_3 eigenvalue $e^{i\pi/3}$.

These two invariants are related to the Wilson loop (WL) spectra of the bands [19], which, due to the presence of crystalline symmetries, can be computed using the corresponding eigenvalues. We will use ν_{inv} to characterize finite geometries that retain the same point group as the monolayer ($\bar{3}m$). We will also explore the case of a system in which inversion symmetry is absent, leaving $3m$ as the point group of the structure. For this configuration, $\nu_{no\ inv}$ is the appropriate invariant to describe the topological properties. The inversion-breaking scenario requires further elaboration because we are reducing the number of crystalline symmetries. To relate the topological classification developed to date for SG 164 to this reduced case, we must study how the irreps of this SG map to the SG without inversion, which is SG 156 ($P3m1$). As this is a subgroup of index 2 of

	$\#M_{-1}^I$	$\#\Gamma_{-1}^I$	$\#K_{-1}^3$	$\#\Gamma_{-1}^3$	ν_{inv}
ZrSe ₂	24	24	14	14	(0, 0)
ZrS ₂	14	14	8	6	(0, 2)
SnS ₂	8	8	10	8	(0, 2)
	$\#K_{e^{i\pi/3}}^3$	$\#\Gamma_{e^{i\pi/3}}^3$	$\#K_{-1}^3$	$\#\Gamma_{-1}^3$	$\nu_{no\ inv}$
ZrSe ₂	15	15	14	14	(0, 0)
ZrS ₂	8	9	8	6	(-1, 2)
SnS ₂	8	9	10	8	(-1, 2)

TABLE II. Symmetry indicator invariants related to fractional corner charges in SG 164 monolayer unit cell with (top part) and without (bottom part) inversion symmetry.

SG 164, we can employ the subduction procedure, as explained in detail in [2]. The result of this map can be extracted from the Bilbao Crystallographic Server, and for completeness, it is also presented in the Supplementary Information. The main observation is that this map preserves the EBRs and the fragility of the SG 164 bands. Interestingly, bands with stable topology in SG 164 are mapped either to EBRs (if the K_{-1}^3 invariant is zero) or to fragile bands (if the K_{-1}^3 invariant is nonzero) in SG 156. The prevalence of fragility in SG 156 can also be confirmed by the Smith decomposition procedure for this group, as it does not host stable \mathbb{Z}_2 phases that can be diagnosed by symmetry indicators alone (there can, however, exist other stable topological phases, as the system belongs to the class AII of the Altland–Zirnbauer classification [49]).

Table II collects the rotational symmetry indicators for the valence band set of the selected compounds ZrSe₂, ZrS₂, and SnS₂. Non-trivial results are obtained for all cases except ZrSe₂; although the valence bands of ZrSe₂ and ZrS₂ in Figure 2 (a) and (b) are very similar, with the same distribution of fragile and stable bands near the Fermi level, $\nu_{inv} = \nu_{no\ inv} = (0, 0)$ only for ZrSe₂. Thus, ZrS₂ and SnS₂ are good flake candidates, as both have ν_{inv} and $\nu_{no\ inv} \neq 0$. We note that the invariants ν are defined in terms of the eigenvalues of C_3 and inversion symmetry, in opposition to the \mathbb{Z}_2 invariant in the previous section.

As a general result for all the structures studied, we found that all fragile bands present a zero M_{-1}^I invariant, which indicates a nonwinding Wilson loop along the $\Gamma - M$ direction. This is the usual path for the characterization of the \mathbb{Z}_2 topology and indicates that fragile bands will show a trivial character along that direction even when their WL spectra are calculated in isolation from other bands. Nevertheless, as has been made patent in previous works [11], fragility can be captured by other different paths, a fact that the nonzero values of $K_{e^{i\pi/3}}^3$ and K_{-1}^3 corroborate. These invariants are related to the path $\Gamma - K$, which implies that fragile bands have non-trivial features that will show in responses related to these indicators, such as corner charges. Fragile topology is the main source of these effects in both symmetry

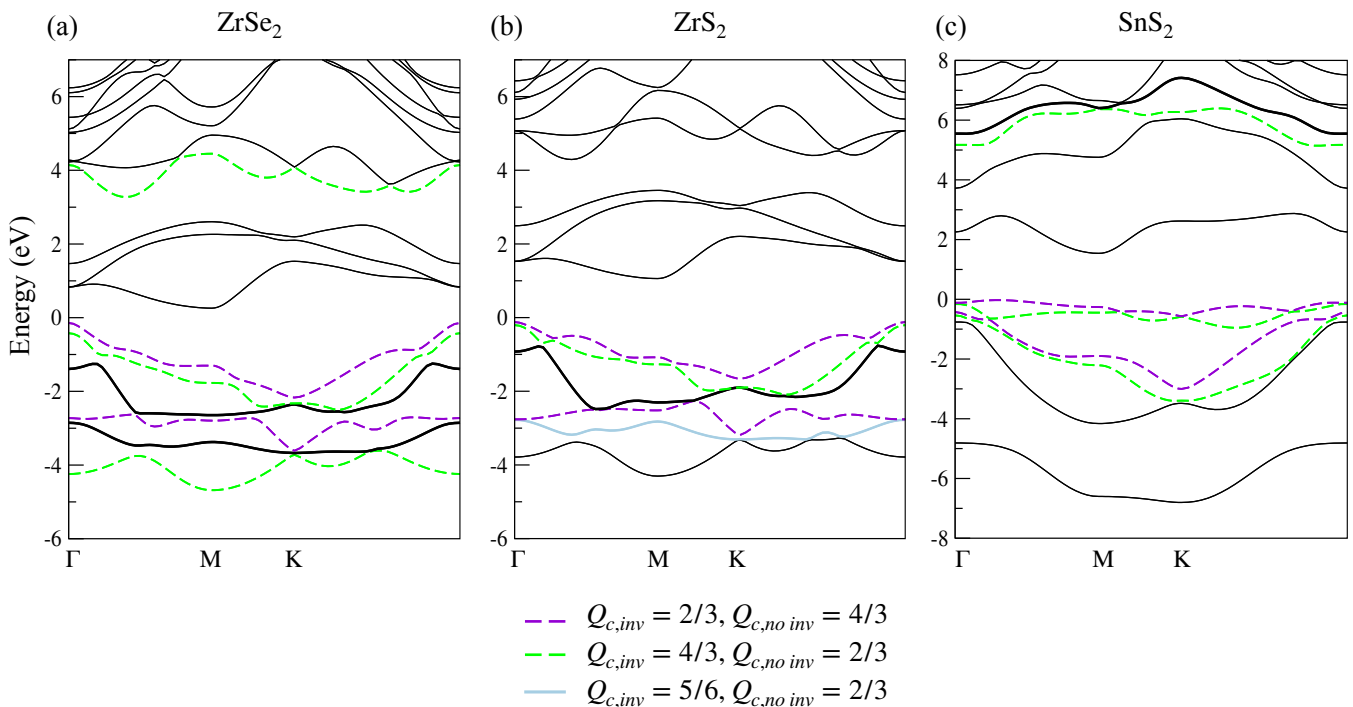


FIG. 3. Band structure of monolayer (a) ZrSe_2 , (b) ZrS_2 and (c) SnS_2 with bands with nonzero partial corner charges colored in green and purple, respectively. Bands with poorly defined corner charges are colored gray. Fragile bands are represented with dashed lines, and stable topological bands are highlighted with thick lines.

configurations, as we will further discuss in the following section.

IV. CORNER CHARGE ANALYSIS

The presence of corner charges is associated with higher-order topology, fragile topology, and even topological crystalline insulators [50]. In an open system, fractional corner charges are a signature of topology that stem from the concept of boundary-obstructed topology [51]. These systems can be trivial under periodic boundary conditions, but not under open conditions. This is consistent with the trivial nature of the valence bands of our database compounds, in opposition to the non-trivial symmetry indicator invariants proposed in Section III B. Corner charges have been shown to be robust against trivialization [25]. In this way, the 'fragility' of these bands can be overcome in an open boundary system. Because the well-known experimental signatures of topological insulators, such as linearly dispersive surface or edge states, are absent in fragile topology, the existence of measurable corner charges is key for the experimental identification of these systems.

In 3D, higher-order topology and fragile topology are easily distinguished because they are described by different symmetry invariants: HOTIs are characterized by an invariant $\mathbb{Z}_4 = 2$, and fragile bands have $\mathbb{Z}_2 = \mathbb{Z}_4 = 0$ but differ from trivial bands in that they cannot be ex-

pressed in terms of EBRs with positive integer coefficients. In 2D, however, HOTIs can only be second-order TIs, and invariants like those of Section III B are used in a general way. In fact, some HOTIs that display corner modes are referred to as fragile [17, 25, 52]. However, most articles on corner charges link them to higher-order topology, namely, second-order topology. Since both stable and fragile bands are present in our system, we aim to know whether the potential (well-defined) corner states are exclusively related to fragile topology or not. To this aim, we suggest two equivalent approaches. First, we follow [19] and compute the total value of the corner charges for the complete valence band set. In particular, in the presence of C_3 and inversion symmetry, the corner charge $Q_{c,inv}$ will be defined as

$$Q_{c,inv} = -\frac{1}{4}M_{-1}^I - \frac{1}{3}K_{-1}^3 \bmod 2 \quad (6)$$

The allowed charge values for the three equal threefold symmetric corners, besides zero, are $2/3$ or $4/3$ [19]. In the absence of inversion, the corner charge $Q_{c,no inv}$ reads

$$Q_{c,no inv} = \frac{2}{3}K_{e^{i\pi/3}}^3 + \frac{2}{3}K_{-1}^3 \bmod 2 \quad (7)$$

This implies six equal corner charges with values $1/3$, $2/3$, 1 , $4/3$, or $5/3$.

These formulas hold in the presence of spin-orbit coupling. In this way, it is possible to select candidate materials and obtain corner charges $Q_{c,inv}$ and $Q_{c,no inv}$ in

$Q_{c,inv}$	$Q_{c,no\ inv}$	Material (TMD)	Material (non-TMD)
4/3	2/3	ZrS ₂ , ZrO ₂ , PdS ₂ , CdI ₂ , PtS ₂ , PtO ₂ , ZnI ₂ , ZnCl ₂ , ZnBr ₂	SnS ₂ , MgI ₂ , MgBr ₂ , GeI ₂ , SnI ₂ , PbI ₂ , CaI ₂ , GeS ₂
0	0	ZrSe ₂ , PtTe ₂ , PtSe ₂ , NiTe ₂ , PdSe ₂	SiSe ₂

TABLE III. Corner charges with and without inversion symmetry of all the materials studied in the database.

a straightforward way from standard first-principles calculations.

Second, to provide a clearer perspective on the relationship between fragility and the presence of corner charges, we compute a partial corner charge, which is the application of the above equations for $Q_{c,inv}$ and $Q_{c,no\ inv}$ to each set of doubly degenerate bands. Thus, we can identify which bands contribute to the total corner charge, and if they have nontrivial topology. This will yield a more detailed explanation of the origin of the total corner charge, since this total magnitude results from the addition (modulo 2) of the partial corner charges.

We first present the result of this last approach in panels (a), (b), and (c) of Figure 3 for ZrSe₂, ZrS₂ and SnS₂, respectively. It can be observed that all three materials present fragile bands with well-defined nonzero corner charges $Q_{c,inv}$ and $Q_{c,no\ inv}$ near the Fermi level, which could be accessed individually in principle by doping processes. Analogous figures for semimetallic examples ZrTe₂ and NiTe₂ can be found in the Supplementary Information.

In Table I we present a summary of the two defined partial corner charges for the sixteen types of basic band representations. It can be readily observed that EBRs do not carry any partial corner charges, and all the nonzero values come from fragile and topologically stable bands. In particular, in the case with no inversion, as only fragile bands are present in SG 156, a nonzero total corner charge is exclusively associated with the presence of uncompensated (fragile) partial corner charges.

On the other hand, when inversion is present, an extra distinction arises between the BRs with nontrivial topology. That is, fragile bands individually have a well-defined fractional corner charge according to the definition [18, 19]. In contrast, bands with stable topology present charges with fractional values that are not allowed by definition, and thus could not give rise to the corresponding filling anomaly. This is the case, for example, of the fifth valence band of ZrS₂ in Figure 3 (b). Crucially, if we consider the formal addition of topologically stable bands, as can be expected when considering the whole valence band manifold, we note that the sum of an even number of stable bands (which will trivialize the \mathbb{Z}_2 invariant) will result in a set of bands that is effectively equivalent to the direct sum of EBRs and fragile bands. If the partial corner charges of the stable bands are now taken as a formal value, we can add these stable bands to compute an effective joint corner charge. The result of this sum is now, remarkably, a well-defined partial corner charge. This reinforces the former statement that an even number of strong bands is equivalent to a

combination of EBRs and fragile bands. We have checked that for all pairwise additions of strong bands in Table I the result is always in the form described above. For instance, if we consider the sum of the fifth and eighth stable bands in this table, both present in ZrS₂, we could express the combination as

$$\begin{aligned} S5 + S8 &= \bar{\Gamma}_9, \bar{M}_3\bar{M}_4, \bar{K}_6 \oplus \bar{\Gamma}_8, \bar{M}_5\bar{M}_6, \bar{K}_4\bar{K}_5 \\ &= \bar{\Gamma}_9, \bar{M}_5\bar{M}_6, \bar{K}_6 \oplus \bar{\Gamma}_8, \bar{M}_3\bar{M}_4, \bar{K}_4\bar{K}_5 = \text{EBR} + \text{F3} \end{aligned} \quad (8)$$

This set now has a corner charge $Q_{c,inv} = 4/3$, which is a well-defined value and the same as that of F3. It follows that the origin of the corner charges in this SG is strongly related to the fragile topology, even when the $\mathbb{Z}_2 = 1$ bands are considered. If the whole valence-band manifold is trivialized, the presence of fragile bands ensures the appearance of corner states as long as the fragile-induced partial corner charges do not cancel each other.

We have checked that the sum of partial charges equals the corner charge obtained by applying equations 6 and 7 for the whole set of valence bands. The results for all the valence bands for each material are gathered in Table III. For all materials in our database, well-defined corner charges $Q_{c,inv} = 4/3$ or $Q_{c,inv} = 0$, and $Q_{c,no\ inv} = 2/3$ or $Q_{c,no\ inv} = 0$ are found, except for ZrTe₂, that has an ill-defined $Q_{c,inv} = 5/6$. This is consistent with the fact that the valence set of ZrTe₂ has a topology of $\mathbb{Z}_2 = 1$. We note that since this material is semimetal, different values could be obtained by choosing a different number of filled bands. Moreover, nearly 74% of the samples have non-zero corner charges, for both TMD and non-TMD materials. Besides the three highlighted systems, other materials with nonzero fractional charges are PdS₂, SnS₂, SnI₂, PbI₂, PtS₂, PtTe₂ and GeI₂, which are synthesized in monolayer form and constitute interesting experimental candidates for STM measurements of corner charges.

V. CORNER STATES IN FLAKES

In contrast to most materials hosting fragile topology, SG 164 does not have C_{2z} symmetry, so our fragile bands must be protected by other symmetry operations. Following our reasoning in previous sections, we propose two flake geometries, a hexagonal one with C_3 symmetry and inversion, and a triangular one with C_3 but without inversion. The latter is the most simple approach since the flake breaks not only the inversion but also the C_2 symmetries, having point group symmetry $3m$. For its part, the hexagonal flake preserves all monolayer symmetries, with point group symmetry $-3m$.

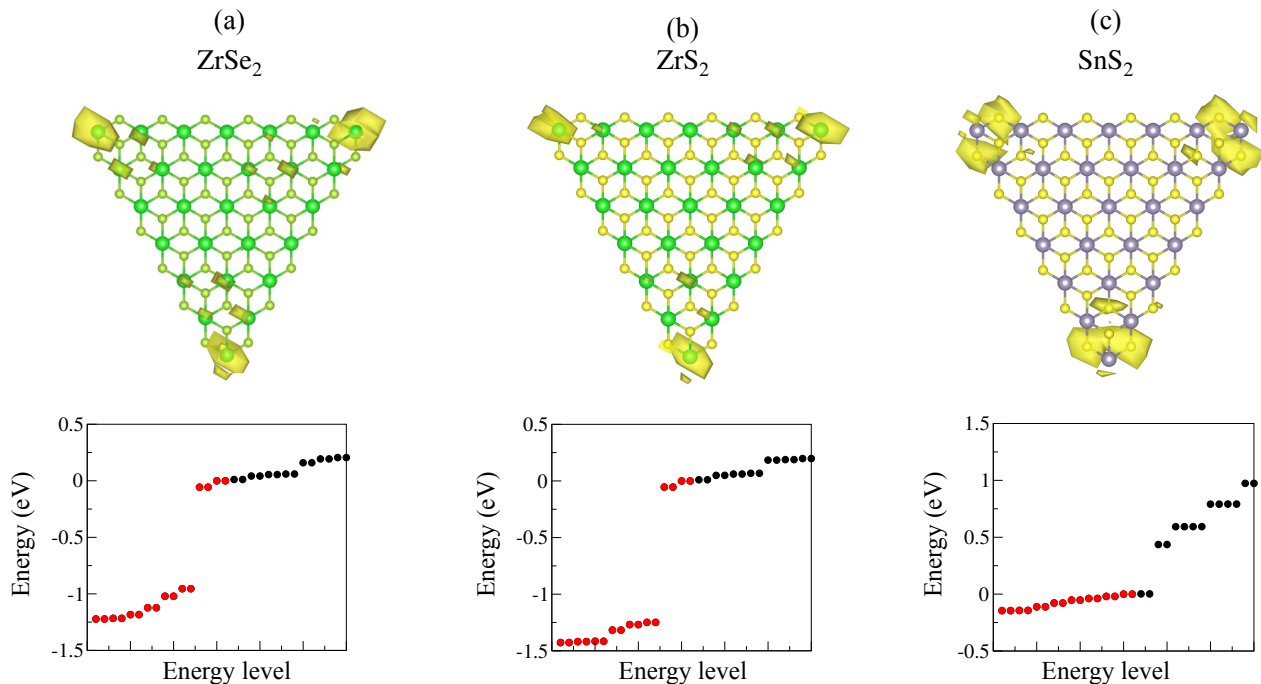


FIG. 4. LDOS (top panel) and eigenvalue spectra (bottom panel) for the (a) ZrSe_2 , (b) ZrS_2 and (c) SnS_2 triangular flakes.

A. Triangular flakes

For the triangular flake, a high electronic localization is observed via the local density of states (LDOS) at the three corners of Figure 4 for the selected materials ZrSe_2 , ZrS_2 , and SnS_2 . Similar calculations are shown for ZrTe_2 and NiTe_2 in the Supplementary Information.

In the bottom panel, the eigenstates for the open system depict an approximate four-fold degeneracy at the Fermi level. Note that the states are not exactly localized at the Fermi level due to the absence of chiral symmetry in real systems [21]. DFT simulations also take into account potential interactions between corner states [53], which contribute to the elimination of degeneracy. This size effect is reduced by increasing the flake size. To fill this four-fold degeneracy, two additional electrons are needed for each material; therefore, each corner of the triangle should contribute $2/3$ to the extra charge needed. Both ZrS_2 and SnS_2 have a corner charge without inversion $Q_{c, no\ inv} = 2/3$, as shown in Table II. The only exception is ZrSe_2 , whose corner charge is 0 for all valence bands. In this case and as commented on in Section IV, since partial corner charges are additive, sometimes the sum of $2/3$ and $4/3$ corner charges, modulo 2, can be zero, as we find in ZrSe_2 . However, since the LDOS calculations only take into account a small energy window near the Fermi energy, corner states are present despite the system having a total corner charge equal to zero. This broadens the set of experimentally realizable materials in the studied SG.

B. Hexagonal flakes

Figure 5 shows the LDOS and energy spectra of the hexagonal flake. Even though this flake preserves all the symmetries of the monolayer, the states near the Fermi energy are not localized in the corners. This is consistent with the findings in Ref. [19], where symmetry-indicator invariants in some obstructed atomic limit phases could be trivialized due to the threefold folding of the original BZ, which folds the K high symmetry points onto Γ [19]. Thus, the symmetry indicator invariants shown in Table II change from $(0, 2)$ for ZrS_2 and SnS_2 and $(0, 0)$ for ZrSe_2 , to $(0, 0)$ for all cases. It follows that no additional fractional charges are needed to overcome any filling anomaly. This argument is also consistent with the eigenvalue spectra, where no half-filled levels appear for any of the three materials.

The LDOS in Figures 5 (a) and (b) depict this lack of corner charges. Panel (c) shows an overall broad extension of the states near the Fermi level along the hexagonal edges. The states signaled by the last two red dots are located throughout all edges. If we compare the lower panels (a) and (b) with (c), we notice that the fourfold degeneracy present in ZrSe_2 and ZrS_2 is broken in SnS_2 . In SnS_2 , edge states arise when the monolayer is cut in a hexagonal geometry. Edge states have also been reported in other materials with C_3 symmetry [31, 33, 34].

Comparing Figures 4 and 5, we conclude that these corner states are present in flakes where their corners span angles of $\pi/6$, such as triangles, and vanish in cor-

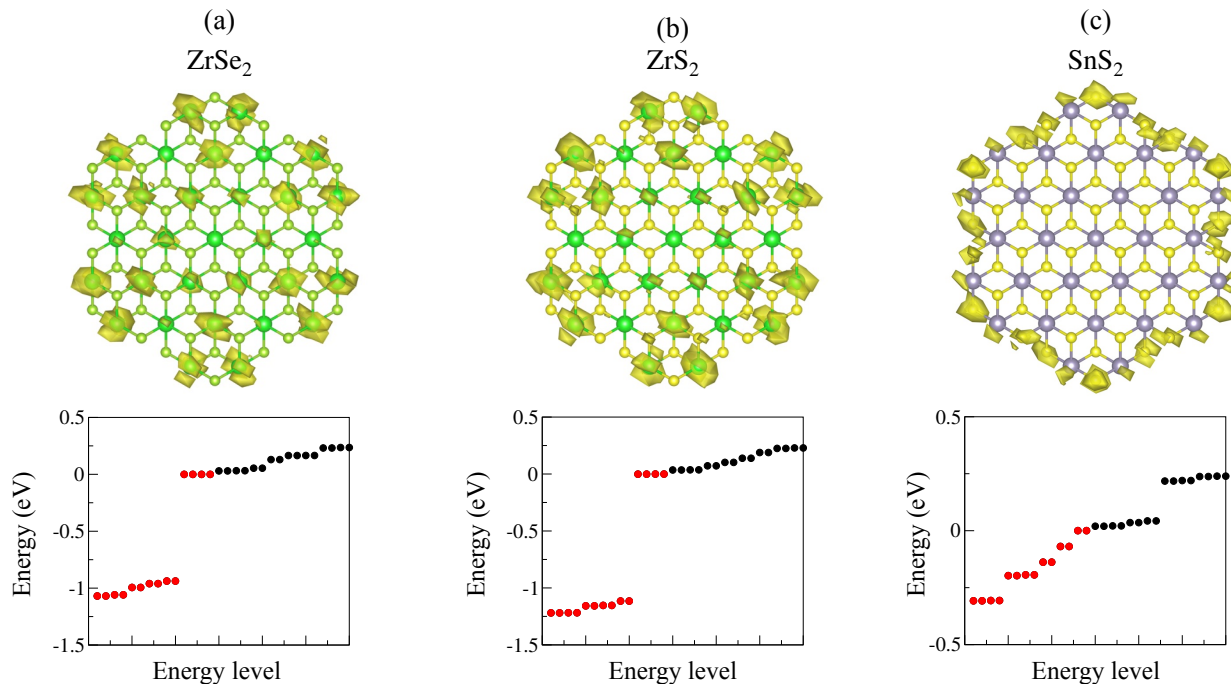


FIG. 5. LDOS (top panel) and eigenvalue spectra (bottom panel) for the (a) ZrSe₂, (b) ZrS₂ and (c) SnS₂ hexagonal flakes.

ners of $\pi/3$, present in hexagons. This behavior has also been recently described in higher-order topological graphene [54]. In summary, our flake calculations show that the corner states in SG 164 are related to a C_3 enforced corner anomaly [54, 55].

VI. CONCLUSIONS

SG 164 monolayer systems span a great variety of structures, which motivates a thorough search for non-trivial topological properties in this family. A comprehensive selection of compounds with the AB₂ formula was surveyed, and the case studies ZrSe₂, ZrS₂ and SnS₂ were selected for a detailed description. Our general results indicate the presence of stable ($\mathbb{Z}_2 = 1$) and fragile topological bands. Thus, SG 164 is an interesting platform to study the interplay between fragile and stable topology and its experimental implications.

Using first-principles calculations, we have analyzed the symmetry eigenvalues of the topologically non-trivial bands in these materials and computed their corner charges and related invariants. We have found nonzero topological indices for more than 70% of the screened materials. A detailed analysis of partial corner charges, computed for each band, has proven fundamental in clarifying the role of stable topological and fragile bands. Whereas these fractional charges are usually related to a higher-order topology, we show that, in SG 164, corner charges stem from fragile bands. Moreover, via ir-

rep subduction to the SG 156, we demonstrate that the non-trivial character of the fragility-induced topological invariants must be preserved in configurations where inversion is explicitly broken.

These findings were tested using triangular and hexagonal geometries. For triangular flakes, a filling anomaly was identified for the three exemplary materials, resulting in a corner charge valued $2/3$. Regarding hexagonal structures, the symmetry indicators are trivialized due to the geometry of the system and the type of obstructed phase associated with the bulk, as previously reported in [19]. However, it is precisely this condition of the nonexistence of corner charges in hexagonal systems that allows the exclusive role of fragile topology in the emergence of charges for triangular systems.

It can also be noted that as the nontrivial results depend on the $3m1$ symmetry, materials with a bulk structure described by SG 156 are likely to present the same effects. Examples of this are Janus TMDs, which are seen as an attractive platform for extending and applying the results achieved in this work.

In summary, a direct link was established between C_3 symmetry-protected corner charges and fragile topology in a wide set of two-dimensional materials. The universality of our findings among SG 164, and possibly other SGs sharing the relevant threefold symmetry, encourages the experimental realization of responses bound to fragile topology in real materials.

ACKNOWLEDGEMENTS

The authors thank J. D. Correa for the helpful discussions. We acknowledge the financial support of the Agencia Estatal de Investigación of Spain under grant PID2022-136285NB and from the Comunidad de Madrid through the (MAD2D-CM)-UCM5 project. OAG acknowledges the support of grant PRE2019-088874 funded by MCIN/AEI/10.13039/501100011033 and by “ESF Investing in your future”. S.B. acknowledges the support of the Postdoctoral Grant from the Universidad T ecnica Federico Santa Mar ıa. M. P. acknowledges the financial support of Chilean FONDECYT by grant 1211913.

APPENDIX: SMITH DECOMPOSITION DATA

We have studied the symmetry invariants of SG 164 two-dimensional materials applying the Smith decomposition procedure [2] to the high-symmetry points in the hexagonal Brillouin zone, depicted in Figure 1 (c) of the main text. Following Ref. [2], an EBR matrix was constructed where the rows indicate all possible irreps of the double space group 164, and the columns display all EBRs. The Smith decomposition allows for the EBR matrix to be re-expressed as

$$\Delta = L \cdot \text{EBR} \cdot R \quad (9)$$

The EBR matrix of the 164 space group monolayer is:

$$\begin{pmatrix} 1 & 0 & 0 & 0 & 1 & 0 & 0 & 0 & 1 & 0 & 1 & 0 & 1 & 0 \\ 0 & 1 & 0 & 0 & 0 & 1 & 0 & 0 & 1 & 0 & 0 & 1 & 0 & 1 \\ 0 & 0 & 1 & 0 & 0 & 0 & 1 & 0 & 0 & 1 & 2 & 0 & 2 & 0 \\ 0 & 0 & 0 & 1 & 0 & 0 & 0 & 1 & 0 & 1 & 0 & 2 & 0 & 2 \\ 1 & 1 & 0 & 0 & 1 & 1 & 0 & 0 & 0 & 1 & 1 & 1 & 1 & 1 \\ 0 & 0 & 1 & 1 & 0 & 0 & 1 & 1 & 2 & 1 & 2 & 2 & 2 & 2 \\ 1 & 0 & 1 & 0 & 1 & 0 & 1 & 0 & 1 & 1 & 1 & 2 & 1 & 2 \\ 0 & 1 & 0 & 1 & 0 & 1 & 0 & 1 & 1 & 1 & 2 & 1 & 2 & 1 \end{pmatrix} \quad (10)$$

And the corresponding Δ matrix:

$$\begin{pmatrix} 1 & 0 & 0 & 0 & 0 & 0 & 0 & 0 & 0 & 0 & 0 & 0 & 0 & 0 & 0 \\ 0 & 1 & 0 & 0 & 0 & 0 & 0 & 0 & 0 & 0 & 0 & 0 & 0 & 0 & 0 \\ 0 & 0 & 1 & 0 & 0 & 0 & 0 & 0 & 0 & 0 & 0 & 0 & 0 & 0 & 0 \\ 0 & 0 & 0 & 1 & 0 & 0 & 0 & 0 & 0 & 0 & 0 & 0 & 0 & 0 & 0 \\ 0 & 0 & 0 & 0 & 1 & 0 & 0 & 0 & 0 & 0 & 0 & 0 & 0 & 0 & 0 \\ 0 & 0 & 0 & 0 & 0 & 2 & 0 & 0 & 0 & 0 & 0 & 0 & 0 & 0 & 0 \\ 0 & 0 & 0 & 0 & 0 & 0 & 0 & 0 & 0 & 0 & 0 & 0 & 0 & 0 & 0 \\ 0 & 0 & 0 & 0 & 0 & 0 & 0 & 0 & 0 & 0 & 0 & 0 & 0 & 0 & 0 \end{pmatrix} \quad (11)$$

The diagonal elements of the Δ matrix indicate that the SG 164 can host Z_2 invariants. This is consistent with

previous works on symmetry-based topological indicators [5, 56]. As mentioned in the main text, this invariant can be computed straightforwardly as:

$$Z_2 = c_6 \bmod 2 \quad (12)$$

Where c_6 is the 6-th element of the c -vector defined as

$$c = L \cdot \Delta \quad (13)$$

If $Z_2 = Z_4 = 0$, bands can be trivial, but they could also be fragile. Thus, when the symmetry indicators are zero, further analysis is needed. This procedure can be performed as part of the Smith decomposition, defining a symmetry data vector containing the irreducible representations [2] and using the BCS data [43]. Note that a Z_2 entry in the matrix Δ does not imply that all materials belonging to SG 164 are Z_2 topological, but that a Z_2 phase is well defined and can appear.

[1] M. G. Vergniory, B. J. Wieder, L. Elcoro, S. S. P. Parkin, C. Felser, B. A. Bernevig, and N. Regnault, All topolog-

ical bands of all nonmagnetic stoichiometric materials, *Science* **376**, eabg9094 (2022).

- [2] L. Elcoro, Z. Song, and B. A. Bernevig, Application of induction procedure and Smith decomposition in calculation and topological classification of electronic band structures in the 230 space groups, *Physical Review B* **102**, 035110 (2020).
- [3] J. Cano and B. Bradlyn, Band Representations and Topological Quantum Chemistry, *Annual Review of Condensed Matter Physics* **12**, 225 (2021).
- [4] H. C. Po, Symmetry indicators of band topology, *Journal of Physics: Condensed Matter* **32**, 263001 (2020).
- [5] H. C. Po, A. Vishwanath, and H. Watanabe, Symmetry-based indicators of band topology in the 230 space groups, *Nature Communications* **8**, 50 (2017).
- [6] F. Schindler, A. M. Cook, M. G. Vergniory, Z. Wang, S. S. P. Parkin, B. A. Bernevig, and T. Neupert, Higher-order topological insulators, *Science Advances* **4**, eaat0346 (2018).
- [7] Z. Song, Z. Wang, W. Shi, G. Li, C. Fang, and B. A. Bernevig, All Magic Angles in Twisted Bilayer Graphene are Topological, *Physical Review Letters* **123**, 036401 (2019).
- [8] H. C. Po, L. Zou, T. Senthil, and A. Vishwanath, Faithful tight-binding models and fragile topology of magic-angle bilayer graphene, *Physical Review B* **99**, 195455 (2019).
- [9] J. Ahn, S. Park, and B.-J. Yang, Failure of Nielsen-Ninomiya Theorem and Fragile Topology in Two-Dimensional Systems with Space-Time Inversion Symmetry: Application to Twisted Bilayer Graphene at Magic Angle, *Physical Review X* **9**, 021013 (2019).
- [10] B. Bradlyn, L. Elcoro, J. Cano, M. G. Vergniory, Z. Wang, C. Felser, M. I. Aroyo, and B. A. Bernevig, Topological quantum chemistry, *Nature* **547**, 298 (2017).
- [11] B. Bradlyn, Z. Wang, J. Cano, and B. A. Bernevig, Disconnected elementary band representations, fragile topology, and Wilson loops as topological indices: An example on the triangular lattice, *Physical Review B* **99**, 045140 (2019).
- [12] J. Cano, B. Bradlyn, Z. Wang, L. Elcoro, M. G. Vergniory, C. Felser, M. I. Aroyo, and B. A. Bernevig, Topology of Disconnected Elementary Band Representations, *Physical Review Letters* **120**, 266401 (2018).
- [13] Z.-D. Song, L. Elcoro, Y.-F. Xu, N. Regnault, and B. A. Bernevig, Fragile Phases as Affine Monoids: Classification and Material Examples, *Physical Review X* **10**, 031001 (2020).
- [14] M. B. de Paz, M. G. Vergniory, D. Bercioux, A. García-Etxarri, and B. Bradlyn, Engineering fragile topology in photonic crystals: Topological quantum chemistry of light, *Physical Review Research* **1**, 032005 (2019).
- [15] J. L. Mañes, Fragile phonon topology on the honeycomb lattice with time-reversal symmetry, *Physical Review B* **102**, 024307 (2020).
- [16] Y. Wei, B. Yan, Y. Peng, A. Shi, D. Zhao, R. Peng, Y. Xiang, and J. Liu, Fragile topology in double-site honeycomb lattice photonic crystal, *Optics Letters* **46**, 3941 (2021).
- [17] B. J. Wieder and B. A. Bernevig, The Axion Insulator as a Pump of Fragile Topology 10.48550/1810.02373 (2018).
- [18] W. A. Benalcazar, T. Li, and T. L. Hughes, Quantization of fractional corner charge in C_n -symmetric higher-order topological crystalline insulators, *Physical Review B* **99**, 245151 (2019).
- [19] F. Schindler, M. Brzezińska, W. A. Benalcazar, M. Iraola, A. Bouhon, S. S. Tsirkin, M. G. Vergniory, and T. Neupert, Fractional corner charges in spin-orbit coupled crystals, *Physical Review Research* **1**, 033074 (2019).
- [20] Z. Wang, B. J. Wieder, J. Li, B. Yan, and B. A. Bernevig, Higher-Order Topology, Monopole Nodal Lines, and the Origin of Large Fermi Arcs in Transition Metal Dichalcogenides XTe_2 ($X = Mo, W$), *Physical Review Letters* **123**, 186401 (2019).
- [21] A. Luo, Z. Song, and G. Xu, Fragile topological band in the checkerboard antiferromagnetic monolayer FeSe, *npj Computational Materials* **8**, 26 (2022).
- [22] S. Kobayashi and A. Furusaki, Fragile topological insulators protected by rotation symmetry without spin-orbit coupling, *Physical Review B* **104**, 195114 (2021).
- [23] S. Kooi, G. Van Miert, and C. Ortix, The bulk-corner correspondence of time-reversal symmetric insulators, *npj Quantum Materials* **6**, 1 (2021).
- [24] Y.-F. Chen and D.-X. Yao, Fragile topological phase on the triangular kagome lattice and its bulk-boundary correspondence, *Physical Review B* **107**, 155129 (2023).
- [25] B. J. Wieder, Z. Wang, J. Cano, X. Dai, L. M. Schoop, B. Bradlyn, and B. A. Bernevig, Strong and fragile topological Dirac semimetals with higher-order Fermi arcs, *Nature Communications* **11**, 627 (2020).
- [26] V. Peri, Z.-D. Song, M. Serra-Garcia, P. Engeler, R. Queiroz, X. Huang, W. Deng, Z. Liu, B. A. Bernevig, and S. D. Huber, Experimental characterization of fragile topology in an acoustic metamaterial, *Science* **367**, 797 (2020).
- [27] D. Rhodes, R. Schönemann, N. Aryal, Q. Zhou, Q. R. Zhang, E. Kampert, Y.-C. Chiu, Y. Lai, Y. Shimura, G. T. McCandless, J. Y. Chan, D. W. Paley, J. Lee, A. D. Finke, J. P. C. Ruff, S. Das, E. Manousakis, and L. Balicas, Bulk Fermi surface of the Weyl type-II semimetallic candidate γ -MoTe₂, *Physical Review B* **96**, 165134 (2017).
- [28] D. Di Sante, P. K. Das, C. Bigi, Z. Ergönenc, N. Gürtler, J. A. Krieger, T. Schmitt, M. N. Ali, G. Rossi, R. Thomale, C. Franchini, S. Picozzi, J. Fujii, V. N. Strocov, G. Sangiovanni, I. Vobornik, R. J. Cava, and G. Panaccione, Three-Dimensional Electronic Structure of the Type-II Weyl Semimetal WTe₂, *Physical Review Letters* **119**, 026403 (2017).
- [29] Y. Wu, N. H. Jo, D. Mou, L. Huang, S. L. Bud'ko, P. C. Canfield, and A. Kaminski, Three-dimensionality of the bulk electronic structure in WTe₂, *Physical Review B* **95**, 195138 (2017).
- [30] F. Schindler, Z. Wang, M. G. Vergniory, A. M. Cook, A. Murani, S. Sengupta, A. Y. Kasumov, R. Deblock, S. Jeon, I. Drozdov, H. Bouchiat, S. Guéron, A. Yazdani, B. A. Bernevig, and T. Neupert, Higher-order topology in bismuth, *Nature Physics* **14**, 918 (2018).
- [31] S. Qian, G.-B. Liu, C.-C. Liu, and Y. Yao, C_n -symmetric higher-order topological crystalline insulators in atomically thin transition metal dichalcogenides, *Physical Review B* **105**, 045417 (2022).
- [32] M. Costa, B. Focassio, L. M. Canonico, T. P. Cysne, G. R. Schleder, R. B. Muniz, A. Fazzio, and T. G. Rappoport, Connecting Higher-Order Topology with the Orbital Hall Effect in Monolayers of Transition Metal Dichalcogenides, *Physical Review Letters* **130**, 116204 (2023).
- [33] G. Liu, H. Jiang, Z. Guo, X. Zhang, L. Jin, C. Liu, and Y. Liu, Magnetic Second-Order Topological Insulators in

- 2H-Transition Metal Dichalcogenides, *Advanced Science* **10**, 2301952 (2023).
- [34] J. Zeng, H. Liu, H. Jiang, Q.-F. Sun, and X. C. Xie, Multiorbital model reveals a second-order topological insulator in 1 H transition metal dichalcogenides, *Physical Review B* **104**, L161108 (2021).
- [35] P. Giannozzi, S. Baroni, N. Bonini, M. Calandra, R. Car, C. Cavazzoni, D. Ceresoli, G. L. Chiarotti, M. Cococcioni, I. Dabo, A. D. Corso, S. de Gironcoli, S. Fabris, G. Fratesi, R. Gebauer, U. Gerstmann, C. Gougoussis, A. Kokalj, M. Lazzeri, L. Martin-Samos, N. Marzari, F. Mauri, R. Mazzarello, S. Paolini, A. Pasquarello, L. Paulatto, C. Sbraccia, S. Scandolo, G. Sclauzero, A. P. Seitsonen, A. Smogunov, P. Umari, and R. M. Wentzcovitch, QUANTUM ESPRESSO: A modular and open-source software project for quantum simulations of materials, *Journal of Physics: Condensed Matter* **21**, 395502 (2009).
- [36] P. Giannozzi, O. Andreussi, T. Brumme, O. Bunau, M. B. Nardelli, M. Calandra, R. Car, C. Cavazzoni, D. Ceresoli, M. Cococcioni, N. Colonna, I. Carnimeo, A. D. Corso, S. de Gironcoli, P. Delugas, R. A. DiStasio, A. Ferretti, A. Floris, G. Fratesi, G. Fugallo, R. Gebauer, U. Gerstmann, F. Giustino, T. Gorni, J. Jia, M. Kawamura, H.-Y. Ko, A. Kokalj, E. Küçükbenli, M. Lazzeri, M. Marsili, N. Marzari, F. Mauri, N. L. Nguyen, H.-V. Nguyen, A. Otero-de-la-Roza, L. Paulatto, S. Poncé, D. Rocca, R. Sabatini, B. Santra, M. Schlipf, A. P. Seitsonen, A. Smogunov, I. Timrov, T. Thonhauser, P. Umari, N. Vast, X. Wu, and S. Baroni, Advanced capabilities for materials modelling with Quantum ESPRESSO, *Journal of Physics: Condensed Matter* **29**, 465901 (2017).
- [37] S. Haastруп, M. Strange, M. Pandey, T. Deilmann, P. S. Schmidt, N. F. Hinsche, M. N. Gjerding, D. Torelli, P. M. Larsen, A. C. Riis-Jensen, J. Gath, K. W. Jacobsen, J. J. Mortensen, T. Olsen, and K. S. Thygesen, The Computational 2D Materials Database: High-throughput modeling and discovery of atomically thin crystals, *2D Materials* **5**, 042002 (2018).
- [38] M. N. Gjerding, A. Taghizadeh, A. Rasmussen, S. Ali, F. Bertoldo, T. Deilmann, N. R. Knøsgaard, M. Kruse, A. H. Larsen, S. Manti, T. G. Pedersen, U. Petralanda, T. Skovhus, M. K. Svendsen, J. J. Mortensen, T. Olsen, and K. S. Thygesen, Recent progress of the Computational 2D Materials Database (C2DB), *2D Materials* **8**, 044002 (2021).
- [39] M. G. Vergniory, L. Elcoro, C. Felser, N. Regnault, B. A. Bernevig, and Z. Wang, A complete catalogue of high-quality topological materials, *Nature* **566**, 480 (2019).
- [40] M. Iraola, J. L. Mañes, B. Bradlyn, M. K. Horton, T. Neupert, M. G. Vergniory, and S. S. Tsirkin, IrRep: Symmetry eigenvalues and irreducible representations of ab initio band structures, *Computer Physics Communications* **272**, 108226 (2022).
- [41] J. M. Soler, E. Artacho, J. D. Gale, A. García, J. Junquera, P. Ordejón, and D. Sánchez-Portal, The SIESTA method for ab initio order-N materials simulation, *Journal of Physics: Condensed Matter* **14**, 2745 (2002).
- [42] A. García, N. Papior, A. Akhtar, E. Artacho, V. Blum, E. Bosoni, P. Brandimarte, M. Brandbyge, J. I. Cerdá, F. Corsetti, R. Cuadrado, V. Dikan, J. Ferrer, J. Gale, P. García-Fernández, V. M. García-Suárez, S. García, G. Huhs, S. Illera, R. Korytár, P. Koval, I. Lebedeva, L. Lin, P. López-Tarifa, S. G. Mayo, S. Mohr, P. Ordejón, A. Postnikov, Y. Pouillon, M. Pruneda, R. Robles, D. Sánchez-Portal, J. M. Soler, R. Ullah, V. W.-z. Yu, and J. Junquera, Siesta: Recent developments and applications, *The Journal of Chemical Physics* **152**, 204108 (2020).
- [43] M. I. Aroyo, A. Kirov, C. Capillas, J. M. Perez-Mato, and H. Wondratschek, Bilbao Crystallographic Server. II. Representations of crystallographic point groups and space groups, *Acta Crystallographica Section A Foundations of Crystallography* **62**, 115 (2006).
- [44] M. I. Aroyo, J. M. Perez-Mato, C. Capillas, E. Kroumova, S. Ivantchev, G. Madariaga, A. Kirov, and H. Wondratschek, Bilbao Crystallographic Server: I. Databases and crystallographic computing programs, *Zeitschrift für Kristallographie - Crystalline Materials* **221**, 15 (2006).
- [45] M. Aroyo, J. Perez-Mato, D. Orobengoa, E. Tasci, G. De La Flor, and A. Kirov, Crystallography online: Bilbao crystallographic server, *Bulgarian Chemical Communications* **43**, 183 (2011).
- [46] M. Zhang, Y. Zhu, X. Wang, Q. Feng, S. Qiao, W. Wen, Y. Chen, M. Cui, J. Zhang, C. Cai, and L. Xie, Controlled Synthesis of ZrS₂ Monolayer and Few Layers on Hexagonal Boron Nitride, *Journal of the American Chemical Society* **137**, 7051 (2015).
- [47] S. Mañas-Valero, V. García-López, A. Cantarero, and M. Galbiati, Raman Spectra of ZrS₂ and ZrSe₂ from Bulk to Atomically Thin Layers, *Applied Sciences* **6**, 264 (2016).
- [48] G. Ye, Y. Gong, S. Lei, Y. He, B. Li, X. Zhang, Z. Jin, L. Dong, J. Lou, R. Vajtai, W. Zhou, and P. M. Ajayan, Synthesis of large-scale atomic-layer SnS₂ through chemical vapor deposition, *Nano Research* **10**, 2386 (2017).
- [49] A. Altland and M. R. Zirnbauer, Nonstandard symmetry classes in mesoscopic normal-superconducting hybrid structures, *Physical Review B* **55**, 1142 (1997).
- [50] Z. Song, Z. Fang, and C. Fang, (d-2) -Dimensional Edge States of Rotation Symmetry Protected Topological States, *Physical Review Letters* **119**, 246402 (2017).
- [51] E. Khalaf, W. A. Benalcazar, T. L. Hughes, and R. Queiroz, Boundary-obstructed topological phases, *Physical Review Research* **3**, 013239 (2021).
- [52] G. Van Miert and C. Ortix, On the topological immunity of corner states in two-dimensional crystalline insulators, *npj Quantum Materials* **5**, 63 (2020).
- [53] B. Liu, G. Zhao, Z. Liu, and Z. F. Wang, Two-Dimensional Quadrupole Topological Insulator in γ -Graphyne, *Nano Letters* **19**, 6492 (2019).
- [54] F. Liu and K. Wakabayashi, Higher-order topology and fractional charge in monolayer graphene, *Physical Review Research* **3**, 023121 (2021).
- [55] C. W. Peterson, T. Li, W. A. Benalcazar, T. L. Hughes, and G. Bahl, A fractional corner anomaly reveals higher-order topology, *Science* **368**, 1114 (2020).
- [56] T. Zhang, Y. Jiang, Z. Song, H. Huang, Y. He, Z. Fang, H. Weng, and C. Fang, Catalogue of topological electronic materials, *Nature* **566**, 475 (2019).